



Thermodynamic Analysis of a Combined Recompression Supercritical Carbon Dioxide Brayton Cycle With an Organic Flash Cycle for Hybrid Solar-Geothermal Energies Power Generation

OPEN ACCESS

Edited by:

Wen Su,
Central South University, China

Reviewed by:

Junjiang Bao,
Dalian University of Technology, China

Lei Gao,
University of Maryland, United States

Yue Cao,
Southeast University, China

*Correspondence:

Yi Que
queyi_sw@cnpc.com.cn
Zhang Jiang
20183313@cqu.edu.cn

Specialty section:

This article was submitted to
Process and Energy Systems
Engineering,
a section of the journal
Frontiers in Energy Research

Received: 20 April 2022

Accepted: 19 May 2022

Published: 03 June 2022

Citation:

Que Y, Hu Z, Ren S and Jiang Z (2022)
Thermodynamic Analysis of a
Combined Recompression
Supercritical Carbon Dioxide Brayton
Cycle With an Organic Flash Cycle for
Hybrid Solar-Geothermal Energies
Power Generation.
Front. Energy Res. 10:924134.
doi: 10.3389/fenrg.2022.924134

Yi Que^{1,2*}, Zhiming Hu¹, Song Ren¹ and Zhang Jiang^{2*}

¹China Petroleum Engineering and Construction Corporation Southwest Company, Chengdu, China, ²Key Laboratory of Low-Grade Energy Utilization Technologies and Systems, Ministry of Education, School of Energy and Power Engineering, Chongqing University, Chongqing, China

Exploring renewable energy is beneficial for ameliorating the energy crisis and reducing environmental emissions. The hybrid utilization of solar and geothermal energies is an effective way to improve the existing energy consumption structure dominated by fossil energy. This paper proposes a novel power generation system composed of a topping recompression supercritical carbon dioxide (sCO₂) Brayton cycle and a bottom organic flash cycle (OFC) driven by the hybrid solar-geothermal energies. The sCO₂ Brayton cycle is driven by the heat from the solar tower system, and the OFC is driven by a part of the heat from CO₂ in the sCO₂ Brayton cycle and another part of the heat from the geothermal water. The corresponding energy and exergy analyses of the proposed combined system are presented. The effects of the five main parameters on the system thermodynamic performance are carried out, which are direct radiation intensity, concentration ratio, sCO₂ pressure ratio, preheater terminal temperature difference, and flash temperature. Results show that the OFC with R245ca has the highest exergy efficiency among the different four fluids. The energy efficiency and exergy efficiency of the total system are 26.03% and 33.38%, respectively, since the energy losses exist in the heliostat field and central receivers. There observes that through the parametric study the parameters of direct radiation intensity and concentration ratio are larger causing better system thermodynamic performance. Through the thermodynamic analysis, there observes the power cycle subsystem has the largest energy loss, while the central receiver possesses the highest among other subsystems.

Keywords: hybrid solar-geothermal energy, supercritical carbon dioxide brayton cycle, organic flash cycle, thermodynamic analysis, combined system

1 INTRODUCTION

With the rapid development of the global economy, energy crises and environmental problems have become major global issues. The exploitation of renewable energies, such as solar, geothermal, biomass, and wind, is one of the potential ways to solve such energy and environmental problems and satisfy the gradually growing electricity demand. It has been reported that the goal of increasing the renewable energy production share has been made, which requires a further 50% increase planned between 2019 and 2024 from 26% of the global share in 2018 (Song et al., 2021). Solar as a widely accessible renewable energy is an indispensable part of the future energy framework, with many promising technologies, like photovoltaic (Mariaud et al., 2017), photothermal (Wang et al., 2020a), and hybrid photovoltaic-thermal (Herrando et al., 2018) technologies. Geothermal is also an attractive renewable resource characterized by its relative stability and reliability and suitable for baseload power generation (Wang et al., 2018a).

The complementary use of different renewable energies can improve its energy utilization efficiency, but it enhances the complexity of energy system design. The integrated utilization of solar and geothermal energies is a potential application way. This conception was firstly proposed in 1975 (Li et al., 2020), and continues to attract attention for different types of energy provision. Many research works about this integrated energy utilization have been reported and are drawing interest. Ayub et al. (2015) studied the thermo-economic performance of a solar-binary geothermal power system. Results found that the proposed system had nearly 6% higher net power output and 2% lower levelized cost of electricity compared with a geothermal organic Rankine cycle (ORC) system. Alirahmi et al. (2020) studied a multi-generation system exploiting geothermal and solar energies. Multi-objective optimization results showed that the exergy efficiency and total unit cost were 30% and 130 \$/GJ under the optimal design conditions, respectively. Al-Hamed and Dincer (2019) proposed a novel solar-geothermal system integrated with an ejector-absorption chiller. They found that the thermal efficiency of the proposed system was up to 53%, and the corresponding COP was about 1.03. Another hybrid power generation system for solar-geothermal application was investigated by Bonyadi et al. (2018), who carried out a techno-economic study. Results found that compared with a typical geothermal plant the proposed system had higher thermal efficiency by 12% and less brine consumption. To sum up, there are many ways of integrated utilization of solar and geothermal energy. The design principle of its energy system mainly depends on the energy demand of the user side. The current research mainly focuses on system structure design, operation parameter optimization, demand side optimization, etc.

In recent years, the supercritical carbon dioxide (sCO₂) Brayton cycle with its advantages of compact volume and high-efficient (Liu et al., 2019) has drawn plenty of attention, including configuration optimization (Gao et al., 2021; Gao et al., 2022), economic and environmental evaluation (Wu et al., 2018; Xiao et al., 2022), dynamic control (Wang et al., 2021a), etc.,

Many research works have been reported focused on the applications of the sCO₂ Brayton cycle in the renewable energy field. For example, Novales et al. (2019) studied the different sCO₂ system structures for concentrating solar power through sensitivity analysis. Results showed that the partial cooling cycle was sensitive to turbine efficiency. A multi-objective optimization focused on the different types of sCO₂ Brayton cycle was conducted by Wang et al. (2018b), who reported inter-cooling and partial cooling types as the most suitable ones applied in solar power tower systems. Yang et al. (2020) established the off-design model of the sCO₂ Brayton cycle for solar power tower application. The interaction effects between thermal storage system, heliostat field, and Brayton cycle at part-load conditions were discussed. Thus, it can be seen that the application of the sCO₂ Brayton cycle in the solar-geothermal fields is of great value (Cao et al., 2022).

In the recompression sCO₂ Brayton cycle, a considerable amount of thermal energy is discharged to the cooling water when the CO₂ is cooled to about 32°C before the compression process. Thus, the sCO₂ Brayton cycle performance could be enhanced by adding an appropriate bottoming cycle to utilize this part of energy (Mishra and Singh, 2018). To further improve the solar energy utilization efficiency, the sCO₂ Brayton cycle is supposed to be integrated with a bottoming cycle, like ORC (He et al., 2012; Wang et al., 2020b; Cai et al., 2021; Wang et al., 2022), transcritical CO₂ cycle (Kochunni and Chowdhury, 2021), refrigerating cycle (Wang et al., 2020c; Wang et al., 2021b), etc., Wang et al. (2016) proposed the combined cycle composed of the sCO₂ Brayton cycle and ORC and studied its thermodynamic performance. They found that the ORC arranged between split point and low-temperature recuperator was the optimal scheme. Manjunath et al. (2018) studied the thermodynamic performance of the sCO₂ Brayton cycle combined with the transcritical CO₂ cycle for shipboard turbine waste recovery. Results found the integrated system improved the net power output by 18% compared with the basic one. In addition, the organic flash cycle (OFC) is another potential way to treat the bottoming cycle in the sCO₂ Brayton cycle, since it can avoid the pinch limitation of traditional ORC and the condensation process in the OFC cooler through conventional coolant at all ambient temperatures. Lee et al. (2016) studied the thermodynamic performance of different OFC system structures, including basic type and double expander type, and compared the system performance with ORC for low-grade waste heat recovery. Wu et al. (2018) studied the integration of the sCO₂ Brayton cycle with OFC. Results found that the combined cycle had advantages in cost and efficiency. The mentioned-above studies are usually needed only one heat source to drive. In the case of hybrid solar-geothermal energy utilization, heat available from the geothermal brine can also be utilized to preheat the bottoming cycle, which motivates the pursuit of further performance improvement in this work.

Nevertheless, until now, limited research works have been done focused on the combination between the sCO₂ Brayton cycle and OFC in the context of hybrid solar-geothermal power generation. In this work, a novel hybrid power generation system powered by solar and geothermal energies is proposed. The

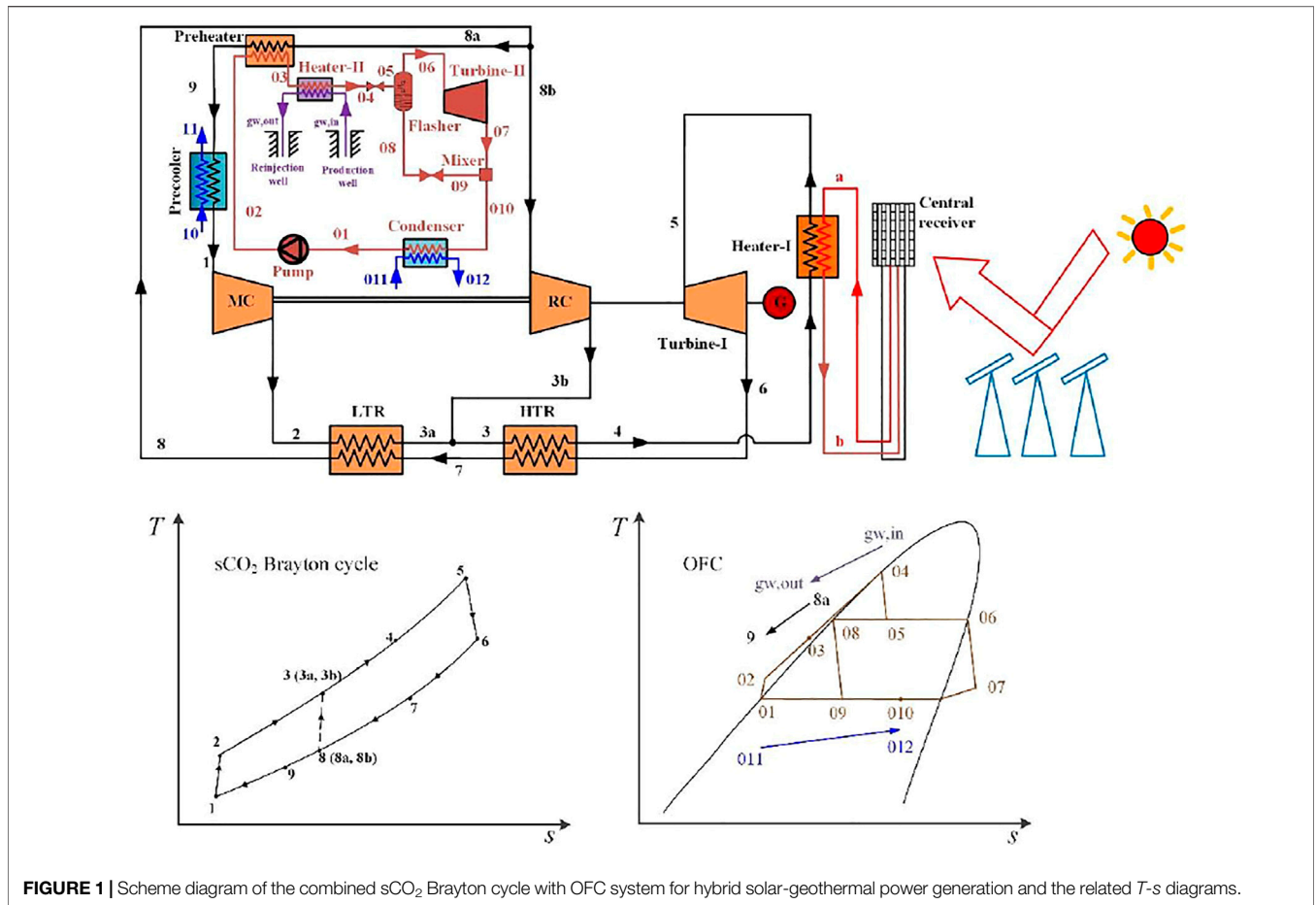


FIGURE 1 | Scheme diagram of the combined sCO₂ Brayton cycle with OFC system for hybrid solar-geothermal power generation and the related T-s diagrams.

hybrid power generation system is composed of the recompression sCO₂ Brayton cycle and OFC. The thermodynamic analysis is conducted to showcase the advantages of the proposed system scheme. The parametric study of the combined sCO₂-OFC system is used to illustrate the effects of important design parameters on thermodynamic performance. The comparative study between different structures and working fluids showcases the advantages of the proposed scheme. The approach assists the design of similar energy cascaded utilization systems, and the obtained results help better design the combined system using sCO₂ and organic fluid.

2 SYSTEM DESCRIPTION

The schematic diagram of the hybrid power generation system is shown in **Figure 1**, which is a topping recompression sCO₂ Brayton cycle and a bottoming OFC. The topping cycle contains two recuperators (named LTR and HTR), two heaters (named Heater-I and Preheater), a cooler (named Precooler), two compressors (named MC and RC), and a turbine (named Turbine-I). The bottoming cycle is composed of a heater (named Heater-II), two valves, a condenser, a flasher, a mixer, a pump, and a turbine (named Turbine-II). The partial heat

released from the sCO₂ Brayton cycle heats the organic fluid in OFC, and then another geothermal stream continues to heat the fluid. The OFC works here to not only utilize the geothermal energy but also strengthen the regenerative effect of the sCO₂ Brayton cycle.

In the topping sCO₂ Brayton cycle, the cooled CO₂ stream (at state point 1) is pressurized by the MC (process 1–2). After that, the high-pressure CO₂ stream (at state point 2) flows through the LTR heated by another CO₂ stream (at state point 7) (process 2–3a) and then mixes with CO₂ stream 3b (process 3a, 3b–3). The merged CO₂ stream (at state point 3) flows through the HTR to be heated by the expanded CO₂ stream (at state point 6) exhausted from the Turbine-I and stream four absorbs the solar heat in the Heater-I (process 4–5). The CO₂ (at state point 5) exiting the Heater-I expands to a low-pressure stream six and generates power in the Turbine-I (process 5–6). The expanded CO₂ stream (at state point 6) continuously flows through the HTR and LTR in turn to heat the high-pressure CO₂ fluid (process 6–7–8). The CO₂ stream (at state point 8) process is split into the main CO₂ stream (at state point 8a) and the bypass CO₂ stream (at state point 8b). The mainstream (at state point 8a) flows through Preheater to drive the bottoming cycle (process 8a–9) and then is cooled by cooling water (process 9–1). Another bypass stream (at state point 8b) is compressed by RC (process 8b–3b) and then merged with CO₂ stream 3a.

In the bottoming OFC, the organic fluid (at state point 01) at the Condenser outlet is pressurized by the Pump (process 01–02). The high-pressure organic fluid (at state point 02) flows through the Heater-II being heated by the hot CO₂ stream (process 02–03). Then, the heated organic fluid (at state point 03) is heated again by the geothermal water to a saturated liquid state (process 03–04). After that, the liquid expands in the valve (process 04–05) to be a two-phase fluid (at state point 05). The fluid is separated into saturated vapor (at state point 06) and saturated liquid (at state point 08) in the flash separator. Then, the vapor (at state point 06) enters the Turbine-II to drive the generator. The liquid (at state point 08) leaving the separator is combined with the expanded flow from Turbine-II (state 06) in the mixer after being decompressed by another valve. Finally, the mixed fluid (at state point 010) flows through the condenser being cooled by the cooling water (process 010–01) before being pressurized by the pump again.

The following reasonable assumptions are made to simplify the simulation:

- 1) The whole system runs under steady-state;
- 2) The heat transfer losses and pressure drops in the heat exchanger and pipe are ignored;
- 3) The fluids in the flash separator and mixer are diabatic and isobaric states, and the throttling valve is isenthalpic equipment.
- 4) Organic fluid at condenser and heater outlets is a saturated liquid state.
- 5) The cooling water at cooler and condenser inlets is under ambient conditions.

3 SYSTEM MODELING

The combined system is modeled by the MATLAB simulation program, including the conservations of mass, energy, and exergy equations for each equipment. The thermophysical properties of all the fluids are obtained from the NIST REFPROP database (Lemmon et al., 2010).

3.1 Solar Tower Subsystem

A typical tower solar power subsystem includes a heliostat field, a central receiver, and molten salt circulation. The heliostat field is used to collect energy from the sun. The energy (Q_{sun}) and exergy (E_{sun}) are defined as

$$Q_{\text{sun}} = DNI \cdot A_h \quad (1)$$

$$E_{\text{sun}} = Q_{\text{sun}} \left[1 - \frac{4T_0}{3T_{\text{sun}}} + \frac{1}{3} \left(\frac{T_0}{T_{\text{sun}}} \right)^4 \right] \quad (2)$$

where DNI is the direct normal irradiance, A_h is the heliostat field area; T_0 is the environment temperature; T_{sun} is the Sun's surface temperature.

The role of the central receiver is to receive the energy reflected from the heliostat field. Based on the literature (Padilla et al., 2015; Herrando et al., 2018; Zhang et al., 2022), the energy

efficiency of the heliostat field (η_{hel}) is set as a constant. Thus the energy (Q_{rec}) and exergy (E_{rec}) absorbed by the central receiver can be expressed as

$$Q_{\text{rec}} = Q_{\text{sun}} \eta_{\text{hel}} \quad (3)$$

$$E_{\text{rec}} = Q_{\text{sun}} \left(1 - \frac{T_0}{T_{\text{sun}}} \right) \quad (4)$$

Besides, the thermal efficiency of the central receiver (η_{rec}) is defined as (Ho and Iverson, 2014; Padilla et al., 2015),

$$\eta_{\text{rec}} = \alpha - \frac{\varepsilon \sigma F_{\text{view}} T_R^4 + f_{\text{conv}} h_{\text{conv}} (T_R - T_0)}{\eta_{\text{hel}} \cdot DNI \cdot C} \quad (5)$$

where α is absorptance, ε is thermal emittance, σ is Stefan Boltzmann constant, F_{view} is radiative view factor; f_{conv} is convective heat loss factor; h_{conv} is convective heat transfer coefficient, T_R is solar receiver temperature, and C is concentration ratio.

In this paper, the shape type of the central receiver is the cavity receiver, molten salt flows through the receiver to absorb heat and transfer it to carbon dioxide. The mixture of 60 wt% NaNO₃ and 40 wt% KNO₃ is selected as the molten salt, and its specific heat is

$$c_{p,\text{ms}} = 0.172T_{\text{ms}} + 1443 \quad (6)$$

where T_{ms} denotes the molten salt temperature.

The energy and exergy equations of molten salt are as follows:

$$Q_{\text{ms}} = Q_{\text{rec}} \eta_{\text{rec}} \quad (7)$$

$$E_{\text{ms}} = m_{\text{ms}} c_{p,\text{ms}} \left[(T_a - T_b) - T_0 \ln \left(\frac{T_0}{T_{\text{sun}}} \right) \right] \quad (8)$$

where m_{ms} is the molten salt mass flow rate, and T_a and T_b are the inlet and outlet temperatures of molten salt.

3.2 sCO₂ Cycle Subsystem

For the sCO₂ cycle subsystem, the exergy balance is defined as

$$E_i = m [(h_i - h_0) - T_0 (s_i - s_0)] \quad (9)$$

where h denotes the enthalpy, s is the entropy, m means the mass flow rate, and the subscript "i" and "0" represent the specific and ambient state points, respectively.

In the Heater-I, the heat absorbed by CO₂ and the corresponding exergy destruction are expressed as the following equations:

$$Q_{\text{Heater-I}} = m_{\text{CO}_2} (h_5 - h_4) \quad (10)$$

$$I_{\text{Heater-I}} = E_{\text{ms}} - (E_5 - E_4) \quad (11)$$

where m_{CO_2} is the CO₂ mass flow rate, and I denotes exergy destruction.

In the Turbine-I, the power output and exergy destruction are defined as

$$Q_{\text{T1}} = m_{\text{CO}_2} (h_5 - h_6) = m_{\text{CO}_2} (h_5 - h_{6s}) \eta_{\text{T1}} \quad (12)$$

$$I_{\text{T1}} = E_5 - E_6 - W_{\text{T1}} \quad (13)$$

where W_{T1} is the power output by the Turbine-I, and η_{T1} is the isentropic efficiency of Turbine-I.

In the HTR, the energy and exergy balance equations, as well as the effectiveness equation, are given as

$$h_6 - h_7 = h_4 - h_3 \quad (14)$$

$$I_{HTR} = E_3 + E_6 - E_4 - E_7 \quad (15)$$

$$\epsilon_{HTR} = (T_6 - T_7) / (T_6 - T_3) \quad (16)$$

where ϵ is the effectiveness efficiency.

In the LTR, the energy and exergy balance equations, as well as the effectiveness equation, are

$$(1 - x)(h_3 - h_2) = h_7 - h_8 \quad (17)$$

$$I_{LTR} = E_{3a} + E_8 - E_2 - E_7 \quad (18)$$

$$\epsilon_{LTR} = (T_7 - T_8) / (T_7 - T_2) \quad (19)$$

where x denotes the CO₂ recompressed flow ratio.

In the Preheater, the CO₂ stream provides heat for the bottoming OFC.

$$Q_{Preheater} = (1 - x)m_{CO_2}(h_{8a} - h_9) = m_{OFC}(h_{03} - h_{02}) \quad (20)$$

$$I_{Preheater} = E_{8a} + E_{02} - E_9 - E_{03} \quad (21)$$

where m_{OFC} is the mass flow rate of organic fluid in the OFC.

In the Precooler, the CO₂ is cooled by the cooling water, and the corresponding energy and exergy equations are

$$Q_{Precooler} = (1 - x)m_{CO_2}(h_9 - h_1) = m_{cw1}(h_{11} - h_{10}) \quad (22)$$

$$I_{Precooler} = E_9 + E_{10} - E_1 - E_{11} \quad (23)$$

where m_{cw1} is the mass flow rate of the cooling water 1.

For the MC and RC, the relative equations are shown as follows

$$PR = P_2 / P_1 \quad (24)$$

$$W_{MC} = (1 - x)m_{CO_2}(h_2 - h_1) = (1 - x)m_{CO_2}(h_{2s} - h_1) / \eta_{com} \quad (25)$$

$$W_{RC} = xm_{CO_2}(h_{3b} - h_{8b}) = xm_{CO_2}(h_{3b} - h_{8b}) / \eta_{com} \quad (26)$$

$$I_{MC} = E_1 - E_2 + W_{MC} \quad (27)$$

$$I_{RC} = E_{8b} - E_{3b} + W_{RC} \quad (28)$$

where η_{com} is the isentropic efficiency of the compressor.

3.3 OFC Subsystem

In the pump, the energy and exergy balance equations are given as

$$Q_{PUMP} = m_{OFC}(h_{02} - h_{01}) = m_{OFC}(h_{02s} - h_{01}) / \eta_p \quad (29)$$

$$I_{PUMP} = E_{01} - E_{02} + W_p \quad (30)$$

where η_p means the isentropic efficiency of the pump.

In the Heater-II, the heat absorbed by organic fluid and the corresponding exergy destruction are expressed as the following equations:

$$Q_{Heater-II} = m_{OFC}(h_{04} - h_{03}) = m_{gw}(h_{gw,in} - h_{gw,out}) \quad (31)$$

$$I_{Heater-II} = (E_{gw,in} - E_{gw,out}) - (E_{04} - E_{03}) \quad (32)$$

where m_{gw} is the mass flow rate of the geothermal water.

In the flash separator, the energy balance equations are:

$$m_{OFC}h_{04} = m_{OFC}h_{05} \quad (33)$$

$$q_{vap} = (h_{05} - h_{08}) / (h_{06} - h_{08}) \quad (34)$$

$$m_{OFC}h_{05} = q_{vap}m_{OFC}h_{06} + (1 - q_{vap})m_{OFC}h_{08} \quad (35)$$

$$I_{Flasher} = E_{05} - (E_{06} + E_{08}) \quad (36)$$

where q_{vap} is the vapor quality of the organic fluid at the flash separator.

In the Turbine-II, the power output and exergy destruction are defined as

$$Q_{T2} = q_{vap}m_{OFC}(h_{06} - h_{07}) = q_{vap}m_{OFC}(h_{06} - h_{07s})\eta_{T2} \quad (37)$$

$$I_{T2} = E_{06} - E_{07} - W_{T2} \quad (38)$$

where W_{T2} is the power output by the Turbine-II, and η_{T2} is the isentropic efficiency of Turbine-II.

In the mixer, the corresponding modeling equations are expressed as

$$q_{vap}m_{OFC}h_{07} + (1 - q_{vap})m_{OFC}h_{09} = m_{OFC}h_{010} \quad (39)$$

$$I_{mixer} = E_{07} + E_{09} - E_{010} \quad (40)$$

For the valve, the exergy destruction is defined as

$$(1 - q_{vap})m_{OFC}h_{08} = (1 - q_{vap})m_{OFC}h_{09} \quad (41)$$

$$I_{valve} = E_{04} - E_{05} + E_{08} - E_{09} \quad (42)$$

In the condenser, the relative equations are expressed as

$$Q_{Condenser} = m_{OFC}(h_{010} - h_{01}) = m_{cw2}(h_{012} - h_{011}) \quad (43)$$

$$I_{Condenser} = E_{010} + E_{011} - E_{01} - E_{012} \quad (44)$$

where m_{cw2} is the mass flow rate of the cooling water 2.

3.4 System Performance Index

The net power output of the proposed sCO₂-OFC system is calculated below:

$$W_{net} = W_{net, sCO_2} + W_{net, OFC} \\ = (W_{T1} - W_{MC} - W_{RC}) + (W_{T2} - W_p) \quad (45)$$

The thermal efficiency of the entire system can be defined as

$$\eta_{th} = W_{net} / (Q_{sun} + Q_{gw}) \quad (46)$$

The exergy efficiency of the proposed system can be expressed as

$$\eta_{ex} = W_{net} / (E_{sun} + E_{gw}) \quad (47)$$

where E_{gw} is the exergy of the geothermal water, which is defined as

$$E_{gw} = E_{gw,in} - E_{gw,out} \quad (48)$$

TABLE 1 | Model validation of sCO₂ Brayton cycle adopting the data reported by S. Mahmoudi et al. (2017).

Items				Split ratio (m_{8a}/m_8)			$\eta_{th}/\%$		
	T_1 (K)	T_5 (K)	P_2 (Mpa)	P_2/P_1	Present work	Ref. (S. Mahmoudi et al., 2017)	RD ^a (%)	Present work	Ref. (S. Mahmoudi et al., 2017)
305.15	823.15	20	2.64	0.3338	0.334	-0.06	41.18	41.18	0
305.15	823.15	30	3.86	0.3549	0.355	-0.02	43.31	43.32	-0.02
323.15	823.15	20	2.40	0.1845	0.184	0.27	36.71	36.71	0
323.15	823.15	30	2.80	0.2541	0.254	0.04	38.93	38.93	0

^aRD means the relative deviation, which is defined as $RD = (x_R - x_S)/x_R \times 100\%$. The x_R and x_S are the values obtained from references and our simulation, respectively.

TABLE 2 | Model validation of OFC adopting the data reported by Tang et al. (2021).

State points	P (kPa)			T (K)			h (kJ/kg)		
	Present work	Ref. (S. Mahmoudi et al., 2017)	RD(%)	Present work	Ref. (S. Mahmoudi et al., 2017)	RD(%)	Present work	Ref. (S. Mahmoudi et al., 2017)	RD(%)
01	249.41	250	-0.24	313.15	313.15	0	252.10	252.57	-0.19
02	1545	1549	-0.26	313.79	313.85	-0.15	253.26	253.82	-0.22
03	1545	1549	-0.26	382.51	382.51	0	354.41	354.80	-0.11
04	789	789	0	353.3	353.15	0.19	354.41	354.80	-0.11
05	789	789	0	353.3	353.15	0.19	462.86	461.75	0.24
06	249.41	250	-0.24	322.83	324.33	-2.93	443.74	444.95	-0.27
07	789	789	0	353.3	353.15	0.19	308.98	309.24	-0.08
08	249.41	250	-0.24	313.15	313.15	0	308.98	309.24	-0.08
09	249.41	250	-0.24	313.15	313.15	0	348.62	349.78	-0.33

4 RESULTS AND DISCUSSIONS

4.1 Model Validation

In this work, the thermodynamic model of the proposed sCO₂-OFC system has been validated to ensure the accuracy of simulation results. The model validation is carried out based on each subsystem, including the sCO₂ Brayton cycle and OFC, and the data from the reported literature (S. Mahmoudi et al., 2017; Tang et al., 2021). A comparison between the data reported by S. Mahmoudi et al. (2017) and our present work for the sCO₂ Brayton cycle is shown in Table 1. In Table 2, the results reported by Tang et al. (2021) and our model are presented about the subsystem of OFC. Referring to comparison results, it can be seen that there is good agreement between our model and it reported in the literature.

4.2 Base Case Study

Based on the subsystem models, the performance of the proposed sCO₂/OFC system driven by solar energy and geothermal energy is explored in this section. The proposed system is set located in Gonghe, Qinghai Province, China, which is full of solar energy and geothermal energy. Moreover, the geothermal energy in Gonghe is the type of hot dry rock (HDR) with a higher temperature and promising application prospect, which is the highest-temperature HDR resource found in China so far (Senqi et al., 2018; Zhang et al.,

TABLE 3 | Design point parameters of the solar tower subsystem (Delussu, 2012; Soo Too and Benito, 2013; Ho and Iverson, 2014).

Subsystem	Parameters	Value
Location	-	36° 6' 8" N
	-	100° 37' 30" E
Heliostat field	Ambient temperature (K)	303.15
	Heliostat field area	12,000 m ²
	Heliostat field efficiency	75%
	Direct normal irradiance (DNI)	800 W/m ²
Central receiver	Absorptance (α)	0.95
	Thermal emittance (ϵ)	0.85
	Radiative view factor (F_{view})	1
	Convective heat loss factor (f_{conv})	1
	Convective heat transfer coefficient (h_{conv})	10 W/m ² K
	Concentration ratio (C)	960
	Solar receiver temperature difference (ΔT_R)	423.15 K
	Molten salt inlet temperature (T_a)	698.15 K
Molten salt outlet temperature (T_b)	858.15 K	

2020). Thus, the geothermal energy used here is considered an enhanced geothermal system (EGS). Table 3 shows the design conditions of the solar tower and HDR-EGS subsystems. The based operation condition of the power subsystem is listed in Table 4.

TABLE 4 | Design point parameters of the EGS and sCO₂-OFC power subsystems (Zhang et al., 2020; Cao et al., 2022; Zhang et al., 2022).

Subsystem	Parameters	Value
EGS	Depth (<i>D</i>)	3705
	Temperature of HDR (<i>T</i> _{HDR})	509.15 K
	Temperature of hot water (<i>T</i> _{g1})	453.15 K
sCO ₂ -OFC power subsystem	Mass flow rate of hot water (<i>m</i> _g)	50 kg/s
	Environment pressure	101.325 kPa
	sCO ₂ minimum pressure	7.4 MPa
	sCO ₂ pressure ration (<i>PR</i>)	3
	sCO ₂ compressor inlet temperature	308.15 K
	sCO ₂ compressor efficiency	85%
	sCO ₂ turbine efficiency	90%
	Heat exchanger efficiencies of recuperator (ϵ_{HTR} and ϵ_{LTR})	0.95
	OFC turbine efficiency	80%
	OFC pump efficiency	75%
Terminal temperature difference in the preheater ($\Delta T_{\text{t, pre}}$)	10 K	

TABLE 5 | Main performance parameters of R245ca.

Working fluid	Molecular mass (g/mol)	<i>T</i> _c (K)	<i>P</i> _c (MPa)	ODP	GWP/100years	Safety level
R245ca	134.05	447.55	3.93	0	726	A2

TABLE 6 | System baseline simulation results.

Subsystems	Energy input (kW)	Energy output (kW)	Energy efficiency (%)	Energy loss ratio ^b (%)	Exergy input (kW)	Exergy output (kW)	Exergy efficiency (%)	Exergy loss ratio ^c (%)
Heliostat field	9600.00	7200.00	75	26.38	8446.10	6817.47	80.72	26.40
Central receiver	7200.00	6225.89	86.47	10.71	6817.47	3751.71	55.03	49.69
Power cycle	8800.00	3076.90	34.96	62.91	4551.90	3076.90	67.60	23.91
Total system	12,174.2 ^a	3076.90	25.27	-	9246.29 ^a	3076.90	33.28	-

^aFor the total system, there is an extra energy input from EGS (2574.2 kW).

^bEnergy loss ratio = Energy loss/Total energy loss ×100%.

^cExergy loss ratio = Exergy loss/Total exergy loss ×100%.

TABLE 7 | System baseline simulation result of the sCO₂-OFC system.

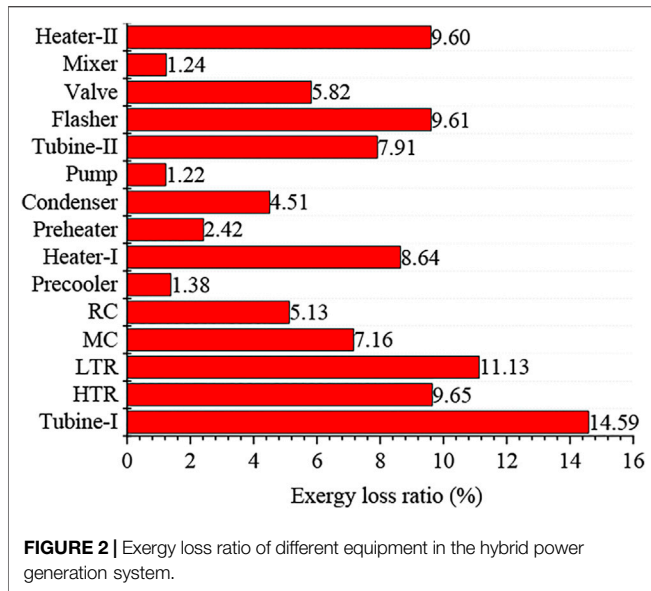
Items	Value
sCO ₂ turbine power output (<i>W</i> _{t, CO2})	4313.58 kW
sCO ₂ main compressor power consumption (<i>W</i> _{mcc})	852.22 kW
sCO ₂ recompressor power consumption (<i>W</i> _{rc})	821.90 kW
sCO ₂ net power output (<i>W</i> _{net, CO2})	2639.45 kW
OFC turbine power output (<i>W</i> _{t, OFC})	510.96 kW
OFC pump power consumption (<i>W</i> _p)	73.52 kW
OFC net power output (<i>W</i> _{net, OFC})	437.44 kW
Power subsystem net power output (<i>W</i> _{net, power})	3076.90 kW
Power subsystem thermal efficiency ($\eta_{\text{th, power}}$)	34.96%
Power subsystem exergy efficiency ($\eta_{\text{ex, power}}$)	67.60%

Besides, R245ca is selected as the working fluid for the OFC system (Cao et al., 2022; Tang et al., 2022). **Table 5** lists the main performance parameters of R245ca working fluids (Calm and Hourahan, 2011). It can be seen that R245ca owns 0 ozone

depletion potential, low global warming potential, and meets the requirements of closed power cycles. In addition, it also has a higher critical temperature which is closed to the EGS temperature.

This section presents the energy and exergy analysis of the proposed system under the base case. **Table 6** lists the thermodynamic performance of the total system, while **Table 7** shows the results of the sCO₂-OFC power subsystem.

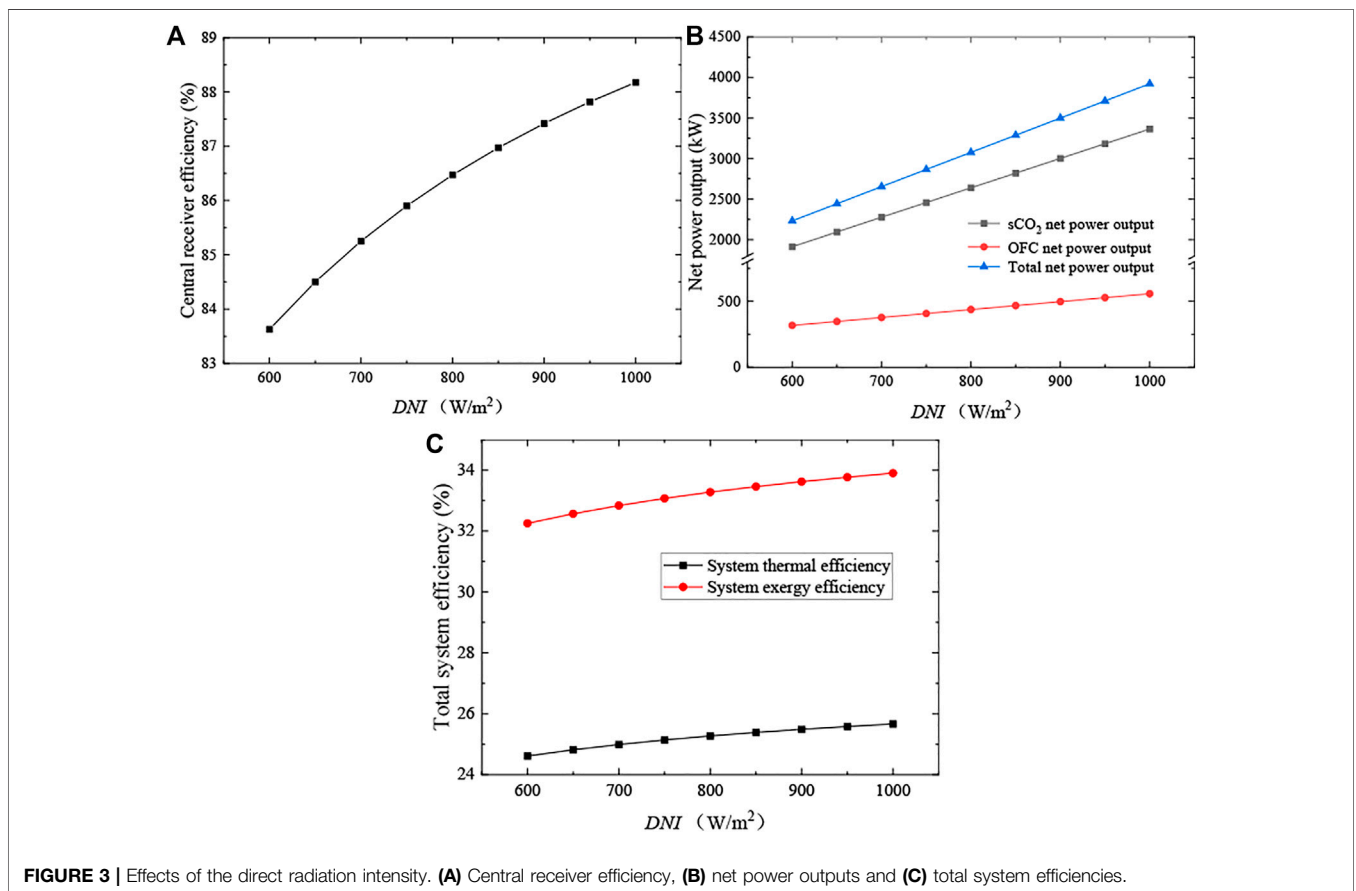
As shown in **Table 6**, under the base condition, the heliostat field can deliver 7200 kW of thermal energy to the central receiver, with all energy input from the sun (9600 kW). It should be noted that the energy input from the EGS system is 2574.2 kW. From the results, it is interesting that the power cycle subsystem has the largest energy loss, accounting for 62.91% of total exergy losses, while it also has the least exergy losses, accounting for only 23.91%. On the contrary, although the central receiver accounts for the least energy loss ratio of 10.71%, its exergy loss is highest among other



subsystems, with a proportion of 49.69%. The reason caused this phenomenon is the working process of the central receiver: the very high-temperature sunlight (~5300 K) is concentrated by the receivers to improve the receiver surface temperature, causing a high-temperature difference. Meanwhile, there still occurs a high-

temperature difference in the energy absorption process between the receiver and molten salts. Therefore, the energy loss in the central receiver has high quality with a big temperature difference and huge heat energy. Referring to **Table 7**, with the total energy input ($Q_{geo} + Q_{ms}$) of 12,174.2 kW, the power subsystem can produce a net power output of 3076.90 kW, which is the sum of sCO₂ net power output (2639.45 kW) and OFC net power output (437.44 kW). The OFC net power output only accounts for 14.2% of total system output. Moreover, the thermal and exergy efficiencies of the power subsystem are 34.96 and 67.60%, respectively, while the corresponding values of the total system are 25.27 and 33.28%, respectively.

In addition, since the relatively high energy and exergy losses of the power cycle subsystem, the exergy loss ratio of each power cycle subsystem's component is presented in **Figure 2**. As shown in **Figure 2**, Turbine-I has the largest exergy losses of 14.59% due to the large mass flow rate of fluids during the expansion process, followed by 11.13% in the HTR and 9.65% in the LTR. In addition, the exergy loss in two heaters (Heater-I and Heater-II) reach 8.64% and 9.60%, respectively, which is mainly caused by the large temperature difference at the heat exchanger inlet and outlet. The large exergy loss in the above components indicates that people should pay more attention to those to improve the system performance. In addition, it is noted



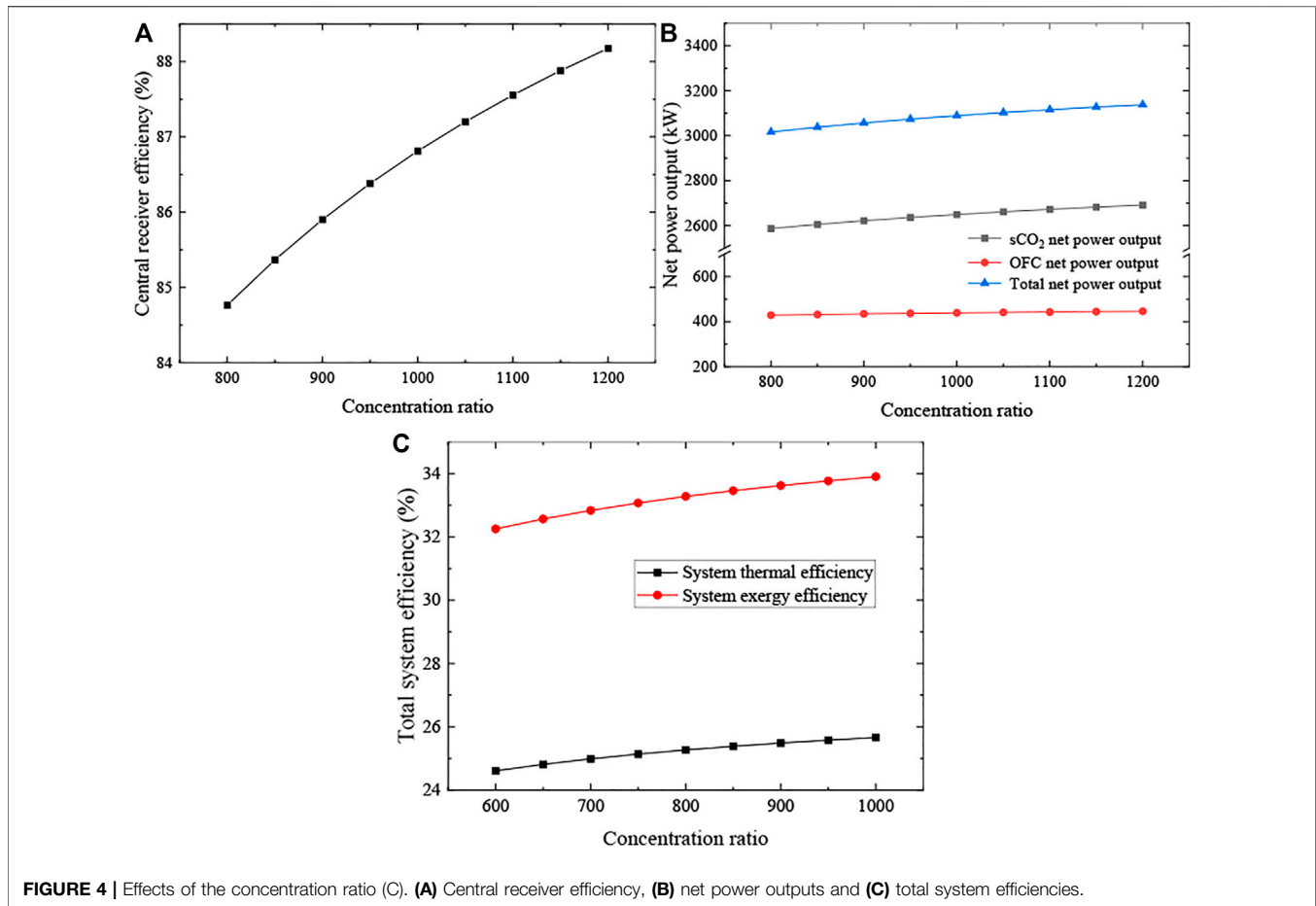


FIGURE 4 | Effects of the concentration ratio (C). **(A)** Central receiver efficiency, **(B)** net power outputs and **(C)** total system efficiencies.

that the component of the sCO₂ cycle has more exergy losses than the OFC cycle.

4.3 Parameter Effect on System Thermodynamic Performance

In this section, it should be noted that the proposed system consists of the solar tower, sCO₂, and OFC subsystems. Hence, the parameters of each subsystem should be considered. The direct normal irradiation (DNI) and the concentration ratio (C) are selected as the key parameters because they directly affect the performance of the heliostat field and central receiver subsystems. Meanwhile, for the power subsystem, both the state points of the sCO₂ cycle and OFC cycle should be considered. Thus, the pressure ratio of the sCO₂ cycle (PR), the pinch point in the preheater (ΔT_{pre}), and the flash temperature (T_{04}) are selected. The former parameter affects the performance of the sCO₂ cycle, while the latter two affect the OFC cycle. The other parameters keep unchanged when one parameter is discussed.

4.3.1 Effect of Direct Radiation Intensity (DNI)

The effects of Direct Radiation Intensity (DNI) are presented in **Figure 3**. As shown in **Figure 3A**, the central receiver efficiency (η_{rec}) increases with the increment of DNI. This is because a large

DNI also means an increasing energy input from the sun (Q_{sun}). In detail, Q_{sun} rises from 7200 kW to 12,000 kW and η_{rec} rises from 83.63% to 88.18% when DNI ranging 600–1000 W/m². Thus, there is also an increment in the net power outputs of sCO₂ and OFC cycles, as shown in **Figure 3B**. The reason for this trend is that a higher Q_{sun} increases the mass flow rate of CO₂ working fluid, then resulting in a higher net power output of the sCO₂ cycle. Meanwhile, the mass flow rate of the OFC cycle also increases with the increasing m_{sCO_2} , so the net power output of the OFC cycle increases as well. As a result, it can be seen in **Figure 3C** that both the total system thermal and exergy efficiencies grow up with a liner increment, under the positive effect of the large increment of net power output.

4.3.2 Effect of Concentration Ratio (C)

Figure 4 shows the effects of concentration ratio (C) on system performance. Similar to DNI, the concentration ratio also has a positive effect on η_{rec} . When C ranges from 800 to 1200, η_{rec} rises from 84.76% to 88.18%, as shown in **Figure 4A**. Then the energy input of the sCO₂ cycle increases as well, causing the increment of m_{sCO_2} . Meanwhile, the state point of the sCO₂ cycle has not been changed. As a result, the net power output of the sCO₂ cycle increases as shown in **Figure 4B**. Meanwhile, the mass flow rate of the OFC cycle also increases with the increasing m_{sCO_2} , so the net power output of the OFC cycle increases as well. With the

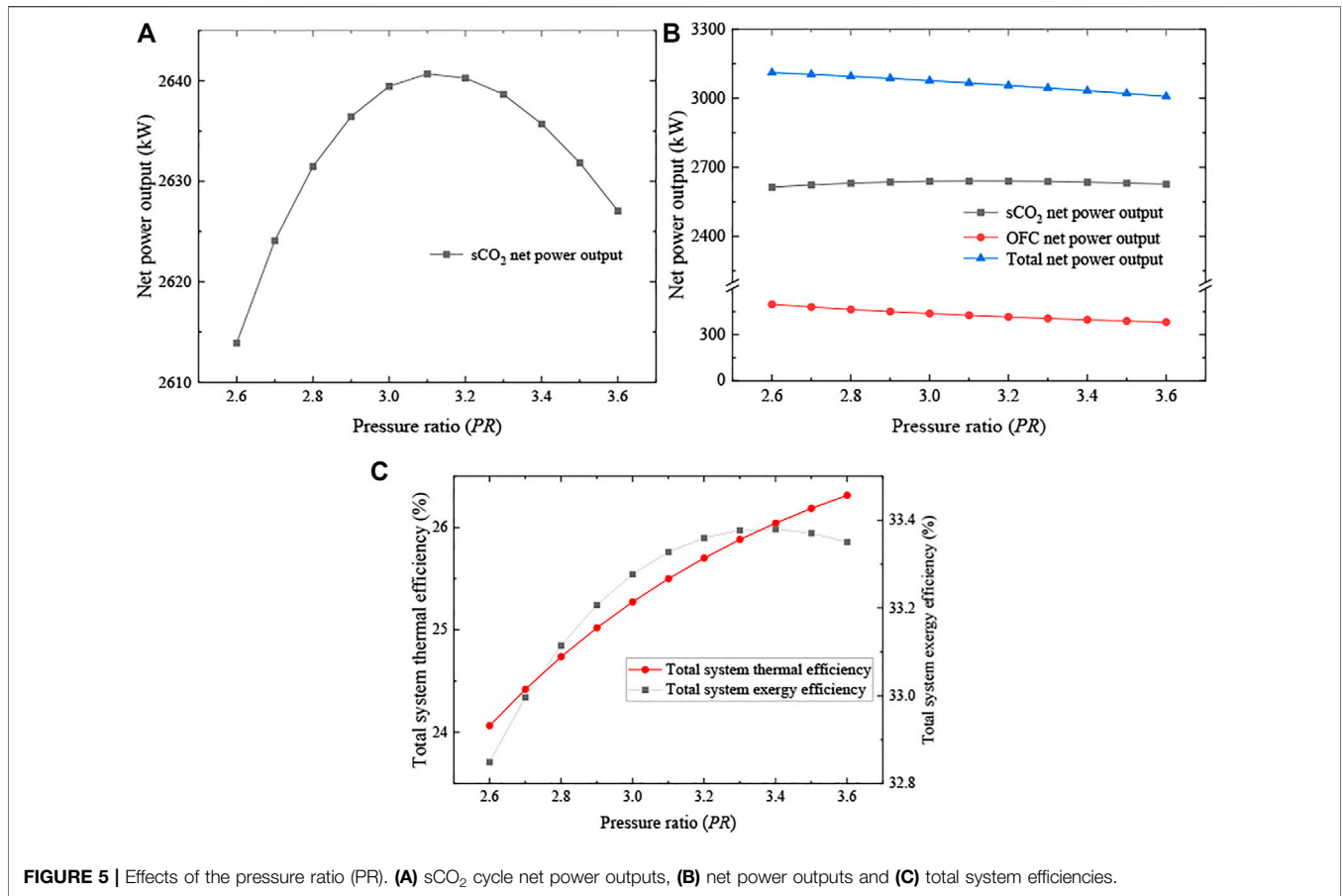


FIGURE 5 | Effects of the pressure ratio (PR). **(A)** sCO₂ cycle net power outputs, **(B)** net power outputs and **(C)** total system efficiencies.

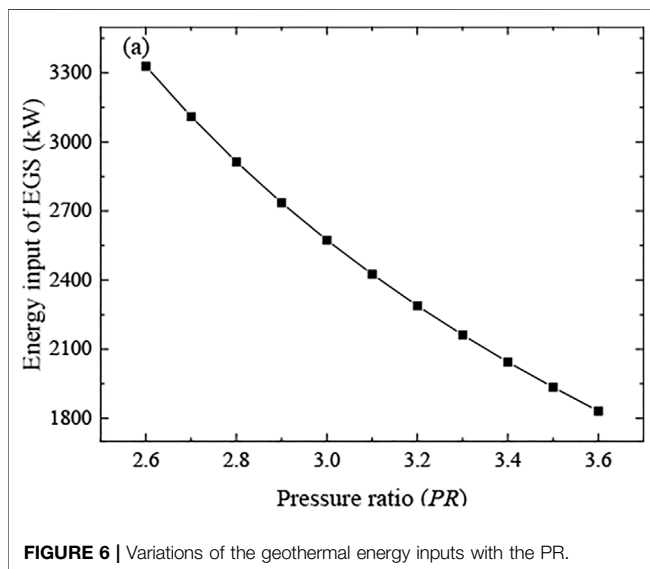


FIGURE 6 | Variations of the geothermal energy inputs with the PR.

increment of total system output, it can be seen from **Figure 4C** that system thermal efficiency grows up from 24.88% to 25.67%, and system exergy efficiency grows up from 32.67% to 33.88%.

4.3.3 Effect of sCO₂ Pressure Ratio (PR)

Figure 5 illustrates the influence of the sCO₂ pressure ratio (PR). As shown in **Figure 5A**, when PR changes from 2.6 to ~ 3.15, W_{net, sCO_2} increases but turns to decrease when PR is beyond 3.15. This is because, for the sCO₂ cycle, a large PR means a high turbine inlet pressure, so the consumption power of the two compressors will increase. Meanwhile, the turbine output also increases under a higher PR. Thus, there is an optimal PR valve for the net power output of the sCO₂ cycle. In **Figure 5B**, it can be seen that the OFC net power output decreases within the range of PR. The reason for this phenomenon is that: a higher PR makes the outlet temperature of LTR (T_8) increase, then increases the OFC working fluid temperature at the preheater outlet. Meanwhile, the mass flow rate of working fluids in the sCO₂ cycle and OFC cycle reduce. Thus, OFC net power output shows a declining trend (from 581.05 to 445.40 kW). The decline of OFC net power output offset the increment of sCO₂ net power output, so net power output decreased.

In addition, the energy input for the geothermal energy reduces as well, from 3328.59 to 1832.19 kW (shown in **Figure 6**). In other words, the total energy is declining fast with the change in PR. As shown in **Figure 5C**, under the combined effect of net power output and energy input, the increment of system efficiencies becomes smaller. In particular, the exergy efficiency reaches the maximum value of about 33.38% with a PR of 3.3.

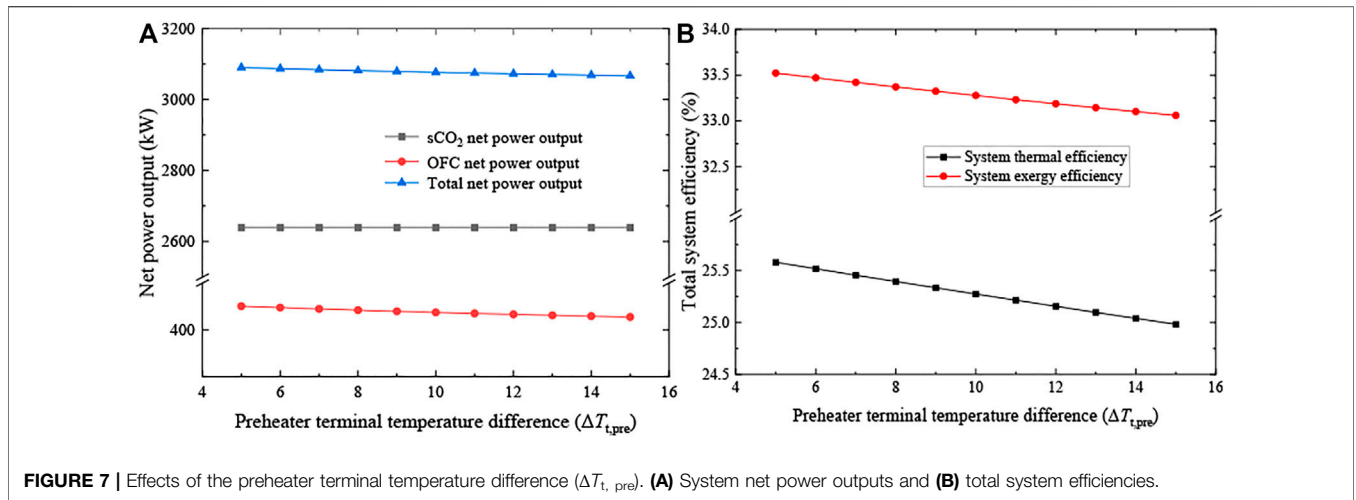


FIGURE 7 | Effects of the preheater terminal temperature difference ($\Delta T_{t,pre}$). (A) System net power outputs and (B) total system efficiencies.

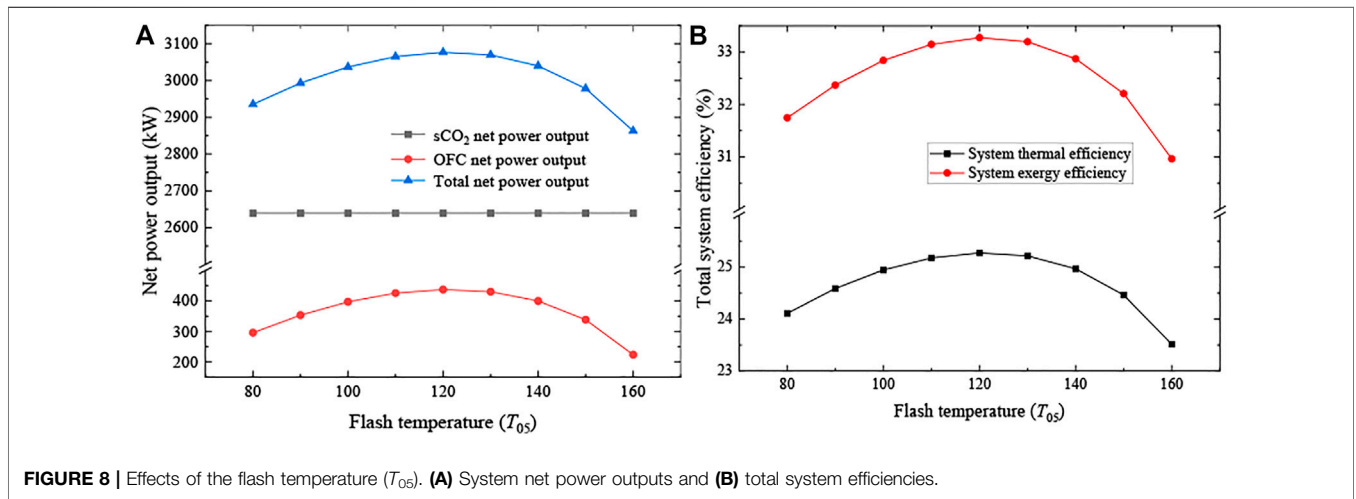


FIGURE 8 | Effects of the flash temperature (T_{05}). (A) System net power outputs and (B) total system efficiencies.

4.3.4 Effect of Preheater Terminal Temperature Difference ($\Delta T_t, Pre$)

Figure 7 shows the influence of preheater terminal temperature difference ($\Delta T_{t,pre}$). As shown in Figure 7A, since the sCO₂ net power output keeps constant, the total net power output decreases with a decreasing OFC net power output. This is because, for the OFC cycle, a large $\Delta T_{t,pre}$ means the heat transfer in the preheater (i.e., the energy input from the sCO₂ cycle to the OFC cycle) gets worse. In other words, the mass flow rate of OFC working fluid reduces as well, resulting in a reduction in the OFC net power output (from 450.63 to 427.55 kW). As a result, as shown in Figure 7B, system energy and exergy efficiencies decrease in a similar decline in net power output, from 25.58% to 24.98% and 33.52%–33.06% respectively.

4.3.5 Effect of Flash Temperature (T_{05})

Figure 8 illustrates the influence of flash temperature (T_{05}) on the system performance. Like $\Delta T_{t,pre}$, the change of T_{05} affects the OFC performance first and then changes the total system performance. In the OFC cycle, T_{05} not only determines the

turbine inlet temperature ($T_{06} = T_{05}$) but also the saturated pressure of the organic working fluid (i.e., the turbine inlet pressure). Namely, the inlet temperature and pressure of the turbine increase when T_{05} arises. On the one hand, a higher turbine inlet pressure contributes to the increasing enthalpy drop of the turbine. On the other hand, the vapor exiting the flasher also drops with an increasing T_{05} , which means the working fluid flowing into the turbine is reduced. There exists a game relationship between the increasing enthalpy drop and decreasing the mass flow of vapor. At first, the positive effect brought by the increasing enthalpy drop can offset the negative effect brought by the decreasing mass flow of vapor, the net power output of OFC increases at a lower T_{05} (below 393.15 K). When T_{05} is beyond 393.15 K, the negative effect dominates the trends of OFC net power output and causes the decline of $W_{net, OFC}$. Therefore, as shown in Figure 8A, there is an optimal T_{04} that can reach maximum OFC net power output as well as that of the total system. In Figure 8B, since the input energy of the total system remains constant, the system efficiencies show similar variation trends when the flash temperature changes.

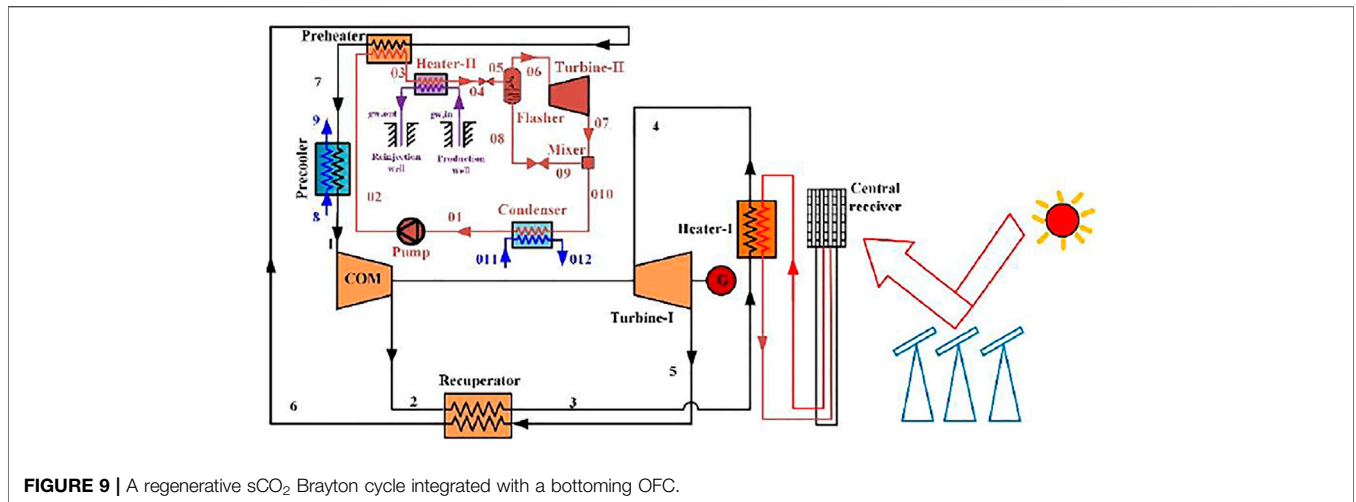


FIGURE 9 | A regenerative sCO₂ Brayton cycle integrated with a bottoming OFC.

TABLE 8 | System performance comparison with two different layouts.

Items	Regenerative sCO ₂ —OFC cycle	Recompression sCO ₂ —OFC cycle
W_{t, CO_2} (kW)	3404.54	4313.58
W_{mc} (kW)	948.61	852.22
W_{rc} (kW)	-	821.90
W_{net, CO_2} (kW)	2455.93	2639.45
$W_{t, OFC}$ (kW)	567.27	510.96
W_p (kW)	81.62	73.52
$W_{net, OFC}$ (kW)	485.65	437.44
$W_{net, power}$ (kW)	2941.58	3076.90
m_{OFC} (kg/s)	23.87	21.44
Q_{geo} (kW)	2828.64	2574.15
$\eta_{th, power}$ (%)	31.63	34.96
$\eta_{ex, power}$ (%)	61.59	67.60
$\eta_{th, tot}$ (%)	23.67	25.27
$\eta_{ex, tot}$ (%)	31.55	33.28

4.4 Comparative Study and Parameter Optimization

In this section, a comparative study is conducted to reveal the difference between different system structures and fluids in the OFC subsystems. After that, the system design parameters are optimized based on the maximum energy efficiency.

4.4.1 Comparison With Different System Layouts

The regenerative sCO₂ Brayton cycle integrated with a bottoming OFC is another normally used way to convert renewable energies into power, as shown in **Figure 9**. To compare the system performance between different structures comprehensively, two commonly used system structures are employed.

The system performance comparison between the two different layouts is listed in **Table 8**. It can be seen that the recompression type has higher power output generated by the sCO₂ cycle, but lower power produced from OFC than the regenerative type. This is because in the recompression type system the top cycle utilizes more energy, while in the regenerative type system more heat is used by the bottom OFC. As for the other parameters, since the recompression type

TABLE 9 | Boundary conditions and settings for optimization.

Items	Value
Population size	50
Generation size	400
Crossover fraction	0.8
Migration fraction	0.2
Stopping criteria	Tolerance <10 ⁻⁴
PR	2.6–3.6
T_5 (°C)	80–160

system generates more power, both the energy efficiency and exergy efficiency of the recompression type system are higher than another system.

4.4.2 System Parameter Optimization and Comparison Between Different Fluids

The discussions of **Section 4.4.1** show the superiority of the combined recompression sCO₂—OFC cycle on the hybrid solar-geothermal energy utilization. Meanwhile, the parametric analysis shows that sometimes, there is an opposite variation trend between the combined

TABLE 10 | The Optimization results for the proposed system with different working fluids.

Fluids	OFC with R245ca	OFC with R123	OFC with MM	OFC with R601a
PR	3.38	3.44	3.39	3.40
T ₅ (°C)	121.49	116.11	109.98	116.47
W _{net, CO₂} (kW)	2636.37	2634.47	2635.95	2635.73
W _{net, OFC} (kW)	398.64	342.56	349.57	370.12
W _{net, power} (kW)	3035.01	2977.03	2985.53	3005.84
m _{OFC} (kg/s)	19.53	26.14	14.18	11.15
Q _{geo} (kW)	2063.93	1869.70	1715.53	1942.44
η _{th, tot} (%)	26.03	25.96	26.02	26.01
η _{ex, tot} (%)	33.38	32.96	33.23	33.20

cycle efficiency and combined cycle net power, which indicates that this variation is related to the utilization of geothermal energy. The increment of net power is on the premise of a significant increase in geothermal energy consumption. Moreover, the parametric analysis also shows the combined system has an optimal value of PR and T₀₅ to achieve maximum energy efficiency.

Hence, this section aims to conduct a performance optimization to find these optimal variables and improve the power generation capacity of the system on the premise of ensuring efficiency. To perform the optimization, the genetic algorithm (GA) is adopted (Gen and Lin, 2007). And the PR and T₀₅ are selected as the decision variables. **Table 9** summarizes the details of boundary conditions and settings for optimization. Moreover, R245ca along with three other working fluids, R123, MM, and R601a is considered to be used in the proposed system.

The system optimization results with four working fluids are listed in **Table 10**. Referring to **Table 10**, the proposed system obtains the total net power outputs of about 2977.03–3035.01 kW and the exergy efficiencies of about 32.96–33.38%. Among the four working fluids, the proposed system with R245ca presents the highest net power output at about 3035.01 kW, followed by R601a, MM, and R123. Due to the higher net power, R245ca also owns the highest exergy efficiency of other fluids. Similarly, the exergy efficiency of the combined system has the same sort of order for the OFC with these four fluids. Moreover, it also can be found that a larger net power of OFC corresponds to a larger absorption of geothermal energy (Q_{geo}), indicating that the employment of geothermal energy is beneficial to power production. At last, the optimization results show that the proposed system with different working fluids can achieve better efficiency under almost the same operating pressure.

5 CONCLUSION AND FUTURE WORK

This paper carried out the thermodynamic analysis of a hybrid solar-geothermal sources powered combined system by introducing an organic flash cycle. The system is composed of a topping recompression sCO₂ Brayton cycle and a bottom OFC. The sCO₂ Brayton cycle is driven by the heat from the solar tower system, and the OFC is driven by a part of the heat from CO₂ in the sCO₂ Brayton cycle and another part of the heat from the geothermal water. The main conclusions are summarized as follows:

- 1) The OFC subsystem with R245ca owns the highest exergy efficiency among involved working fluids. The power output generated by the combined sCO₂-OFC system is 3035.00 kW, including the net power output produced by the sCO₂ cycle of about 2636.37 kW and from the OFC of 398.64 kW. Moreover, the energy efficiency and exergy efficiency of the total system are 26.03% and 33.38%, respectively, since the energy losses exist in the heliostat field and central receivers.
- 2) Through the parametric study, there observes that the values of DNI and C are larger, and the performance of the hybrid power generation system is better. There is an optimal PR and T₀₅, corresponding to the maximum exergy efficiency of the combined system. The system performance is better when the preheater terminal temperature difference is smaller.
- 3) The power cycle subsystem has the largest energy loss, while it also has the least exergy losses. On the contrary, the central receiver accounts for the least energy loss ratio, but its exergy loss is highest among other subsystems.

In the future, a more systematic analysis could be considered, like thermos-economic, environmental, and ecological impacts. Besides, the off-design analysis and dynamic analysis can also be employed to offer guidelines for the utilization of renewable energies in future research.

DATA AVAILABILITY STATEMENT

The original contributions presented in the study are included in the article/supplementary material, further inquiries can be directed to the corresponding authors.

AUTHOR CONTRIBUTIONS

YQ: Conceptualization, methodology, data analysis, paper writing. ZH: Methodology, data analysis. SR: Methodology, data analysis. ZJ: Conceptualization, supervision of the project, and paper writing and reviewing.

FUNDING

The work is supported by the National Natural Science Foundation of China (No. 51506013).

REFERENCES

- Al-Hamed, K. H. M., and Dincer, I. (2019). Investigation of a Concentrated Solar-Geothermal Integrated System with a Combined Ejector-Absorption Refrigeration Cycle for a Small Community. *Int. J. Refrig.* 106, 407–426. doi:10.1016/j.ijrefrig.2019.06.026
- Alirahmi, S. M., Rahmani Dabbagh, S., Ahmadi, P., and Wongwises, S. (2020). Multi-objective Design Optimization of a Multi-Generation Energy System Based on Geothermal and Solar Energy. *Energy Convers. Manag.* 205, 112426. doi:10.1016/j.enconman.2019.112426
- Ayub, M., Mitsos, A., and Ghasemi, H. (2015). Thermo-economic Analysis of a Hybrid Solar-Binary Geothermal Power Plant. *Energy* 87, 326–335. doi:10.1016/j.energy.2015.04.106
- Bonyadi, N., Johnson, E., and Baker, D. (2018). Technoeconomic and Exergy Analysis of a Solar Geothermal Hybrid Electric Power Plant Using a Novel Combined Cycle. *Energy Convers. Manag.* 156, 542–554. doi:10.1016/j.enconman.2017.11.052
- Cai, S., Wu, C., Li, X., and Li, Q. (2021). Effects of Lubricant on Evaporation and Boiling Processes of R1234Ze(E): A Molecular Dynamics Study. *Appl. Therm. Eng.* 193. doi:10.1016/j.applthermaleng.2021.117009
- Calm, J. M., and Hourahan, G. C. "Physical, Safety, and Environmental Data for Current and Alternative Refrigerants," in Proceedings of 23rd international congress of refrigeration (ICR2011) (Prague, Czech Republic 2011, 21–26.
- Cao, Y., Li, P., Qiao, Z., Ren, S., and Si, F. (2022). A Concept of a Supercritical CO₂ Brayton and Organic Rankine Combined Cycle for Solar Energy Utilization with Typical Geothermal as Auxiliary Heat Source: Thermodynamic Analysis and Optimization. *Energy Rep.* 8, 322–333. doi:10.1016/j.egy.2021.11.258
- Delussu, G. (2012). A Qualitative Thermo-Fluid-Dynamic Analysis of a CO₂ Solar Pipe Receiver. *Sol. Energy* 86, 926–934. doi:10.1016/j.solener.2011.12.023
- Gao, L., Cao, T., Hwang, Y., and Radermacher, R. (2021). Graph-based Configuration Optimization for S-CO₂ Power Generation Systems. *Energy Convers. Manag.* 244. doi:10.1016/j.enconman.2021.114448
- Gao, L., Cao, T., Hwang, Y., and Radermacher, R. (2022). Robustness Analysis in Supercritical CO₂ Power Generation System Configuration Optimization. *Energy* 242. doi:10.1016/j.energy.2021.122956
- Gen, M., and Lin, L. (2007). *Genetic Algorithms*. Wiley Encyclopedia of Computer Science and Engineering, 1–15.
- He, C., Liu, C., Gao, H., Xie, H., Li, Y., Wu, S., et al. (2012). The Optimal Evaporation Temperature and Working Fluids for Subcritical Organic Rankine Cycle. *Energy* 38, 136–143. doi:10.1016/j.energy.2011.12.022
- Herrando, M., Ramos, A., Freeman, J., Zabalza, I., and Markides, C. N. (2018). Technoeconomic Modelling and Optimisation of Solar Combined Heat and Power Systems Based on Flat-Box PVT Collectors for Domestic Applications. *Energy Convers. Manag.* 175, 67–85. doi:10.1016/j.enconman.2018.07.045
- Ho, C. K., and Iverson, B. D. (2014). Review of High-Temperature Central Receiver Designs for Concentrating Solar Power. *Renew. Sustain. Energy Rev.* 29, 835–846. doi:10.1016/j.rser.2013.08.099
- Kochunni, S. K., and Chowdhury, K. (2021). Effect of Precooling with Transcritical CO₂ Cycle on Two Types of LNG Boil-Off Gas Reliquefaction Systems. *J. Nat. Gas Sci. Eng.* 89. doi:10.1016/j.jngse.2021.103876
- Lee, H. Y., Park, S. H., and Kim, K. H. (2016). Comparative Analysis of Thermodynamic Performance and Optimization of Organic Flash Cycle (OFC) and Organic Rankine Cycle (ORC). *Appl. Therm. Eng.* 100, 680–690. doi:10.1016/j.applthermaleng.2016.01.158
- Lemmon, E. W., Huber, M. L., and McLinden, M. O. (2010). *NIST Standard Reference Database 23: Reference Fluid Thermodynamic and Transport Properties-REFPROP. 9.0*. Gaithersburg: NIST NSRDS -
- Li, K., Liu, C., Jiang, S., and Chen, Y. (2020). Review on Hybrid Geothermal and Solar Power Systems. *J. Clean. Prod.*, 250. doi:10.1016/j.jclepro.2019.119481
- Liu, Y., Wang, Y., and Huang, D. (2019). Supercritical CO₂ Brayton Cycle: A State-Of-The-Art Review. *Energy* 189. doi:10.1016/j.energy.2019.115900
- Manjunath, K., Sharma, O. P., Tyagi, S. K., and Kaushik, S. C. (2018). Thermodynamic Analysis of a Supercritical/transcritical CO₂ Based Waste Heat Recovery Cycle for Shipboard Power and Cooling Applications. *Energy Convers. Manag.* 155, 262–275. doi:10.1016/j.enconman.2017.10.097
- Mariaud, A., Acha, S., Ekens-Daukes, N., Shah, N., and Markides, C. N. (2017). Integrated Optimisation of Photovoltaic and Battery Storage Systems for UK Commercial Buildings. *Appl. Energy* 199, 466–478. doi:10.1016/j.apenergy.2017.04.067
- Mishra, R. S., and Singh, H. (2018). Detailed Parametric Analysis of Solar Driven Supercritical CO₂ Based Combined Cycle for Power Generation, Cooling and Heating Effect by Vapor Absorption Refrigeration as a Bottoming Cycle. *Therm. Sci. Eng. Prog.* 8, 397–410. doi:10.1016/j.tsep.2018.09.013
- Novales, D., Erkoreka, A., De la Peña, V., and Herrazti, B. (2019). Sensitivity Analysis of Supercritical CO₂ Power Cycle Energy and Exergy Efficiencies Regarding Cycle Component Efficiencies for Concentrating Solar Power. *Energy Convers. Manag.* 182, 430–450. doi:10.1016/j.enconman.2018.12.016
- Padilla, R. V., Soo Too, Y. C., Benito, R., and Stein, W. (2015). Exergetic Analysis of Supercritical CO₂ Brayton Cycles Integrated with Solar Central Receivers. *Appl. Energy* 148, 348–365. doi:10.1016/j.apenergy.2015.03.090
- Senqi, Z., Weide, Y., Dünpeng, L., Xiaofeng, J., and Lisha, H. (2018). Characteristics of Geothermal Geology of the Qiabuqia HDR in Gonghe Basin, Qinghai Province. *Geol. China* 45, 1087–1102.
- S. Mahmoudi, S., Salehi, S., Yari, M., and Rosen, M. (2017). Exergoeconomic Performance Comparison and Optimization of Single-Stage Absorption Heat Transformers. *Energies* 10, 532. doi:10.3390/en10040532
- Song, J., Wang, Y., Wang, K., Wang, J., and Markides, C. N. (2021). Combined Supercritical CO₂ (SCO₂) Cycle and Organic Rankine Cycle (ORC) System for Hybrid Solar and Geothermal Power Generation: Thermoeconomic Assessment of Various Configurations. *Renew. Energy* 174, 1020–1035. doi:10.1016/j.renene.2021.04.124
- Soo Too, Y. C., and Benito, R. (2013). Enhancing Heat Transfer in Air Tubular Absorbers for Concentrated Solar Thermal Applications. *Appl. Therm. Eng.* 50, 1076–1083. doi:10.1016/j.applthermaleng.2012.06.025
- Tang, J., Zhang, Q., Zhang, Z., Li, Q., Wu, C., and Wang, X. (2022). Development and Performance Assessment of a Novel Combined Power System Integrating a Supercritical Carbon Dioxide Brayton Cycle with an Absorption Heat Transformer. *Energy Convers. Manag.* 251. doi:10.1016/j.enconman.2021.114992
- Tang, Z., Wu, C., Liu, C., Xu, X., and Liu, J. (2021). Thermodynamic Analysis and Comparison of a Novel Dual-Ejector Based Organic Flash Combined Power and Refrigeration Cycle Driven by the Low-Grade Heat Source. *Energy Convers. Manag.* 239. doi:10.1016/j.enconman.2021.114205
- Wang, K., Li, M.-J., Guo, J.-Q., Li, P., and Liu, Z.-B. (2018). A Systematic Comparison of Different S-CO₂ Brayton Cycle Layouts Based on Multi-Objective Optimization for Applications in Solar Power Tower Plants. *Appl. Energy* 212, 109–121. doi:10.1016/j.apenergy.2017.12.031
- Wang, M., Zhao, P., Wang, J., Li, H., and Dai, Y. (2016). Conceptual Design and Parametric Study of Combined Carbon Dioxide/organic Rankine Cycles. *Appl. Therm. Eng.* 103, 759–772. doi:10.1016/j.applthermaleng.2016.04.046
- Wang, S., Liu, C., Li, J., Sun, Z., Chen, X., and Wang, X. (2020). Exergoeconomic Analysis of a Novel Trigeration System Containing Supercritical CO₂ Brayton Cycle, Organic Rankine Cycle and Absorption Refrigeration Cycle for Gas Turbine Waste Heat Recovery. *Energy Convers. Manag.* 221, 113064. doi:10.1016/j.enconman.2020.113064
- Wang, S., Liu, C., Li, Q., Liu, L., Huo, E., and Zhang, C. (2020). Selection Principle of Working Fluid for Organic Rankine Cycle Based on Environmental Benefits and Economic Performance. *Appl. Therm. Eng.* 178, 115598. doi:10.1016/j.applthermaleng.2020.115598
- Wang, S., Liu, C., Zhang, C., Xu, X., and Li, Q. (2018). Thermo-economic Evaluations of Dual Pressure Organic Rankine Cycle (DPORC) Driven by Geothermal Heat Source. *J. Renew. Sustain. Energy* 10, 063901. doi:10.1063/1.5034062
- Wang, S., Liu, C., Zhang, S., Li, Q., and Huo, E. (2022). Multi-objective Optimization and Fluid Selection of Organic Rankine Cycle (ORC) System Based on Economic-Environmental-Sustainable Analysis. *Energy Convers. Manag.* 254, 115238. doi:10.1016/j.enconman.2022.115238
- Wang, S., Zhang, L., Liu, C., Liu, Z., Lan, S., Li, Q., et al. (2021). Techno-economic Environmental Evaluation of a Combined Cooling Heating and Power System for Gas Turbine Waste Heat Recovery. *Energy* 231, 120956. doi:10.1016/j.energy.2021.120956
- Wang, X., Li, X., Li, Q., Liu, L., and Liu, C. (2020). Performance of a Solar Thermal Power Plant with Direct Air-Cooled Supercritical Carbon Dioxide Brayton Cycle under Off-Design Conditions. *Appl. Energy* 261. doi:10.1016/j.apenergy.2019.114359
- Wang, X., Wang, R., Bian, X., Cai, J., Tian, H., Shu, G., et al. (2021). Review of Dynamic Performance and Control Strategy of

- Supercritical CO₂ Brayton Cycle. *Energy AI* 5. doi:10.1016/j.egyai.2021.100078
- Wu, C., Wang, S.-s., and Li, J. (2018). Exergoeconomic Analysis and Optimization of a Combined Supercritical Carbon Dioxide Recompression Brayton/organic Flash Cycle for Nuclear Power Plants. *Energy Convers. Manag.* 171, 936–952. doi:10.1016/j.enconman.2018.06.041
- Xiao, T., Liu, C., Wang, X., Wang, S., Xu, X., Li, Q., et al. (2022). Life Cycle Assessment of the Solar Thermal Power Plant Integrated with Air-Cooled Supercritical CO₂ Brayton Cycle. *Renew. Energy* 182, 119–133. doi:10.1016/j.renene.2021.10.001
- Yang, J., Yang, Z., and Duan, Y. (2020). Off-design Performance of a Supercritical CO₂ Brayton Cycle Integrated with a Solar Power Tower System. *Energy* 201. doi:10.1016/j.energy.2020.117676
- Zhang, X., Zhang, T., Xue, X., Si, Y., Zhang, X., and Mei, S. (2020). A Comparative Thermodynamic Analysis of Kalina and Organic Rankine Cycles for Hot Dry Rock: a Prospect Study in the Gonghe Basin. *Front. Energy* 14, 889–900. doi:10.1007/s11708-020-0704-1
- Zhang, Y., Du, Y., Lu, X., Zhao, P., and Dai, Y. (2022). Performance Improvement of a Solar-Powered Recompression Supercritical Carbon Dioxide Cycle by Introducing an Ammonia-Water Cooling-Power System. *Front. Energy Res.* 9. doi:10.3389/fenrg.2021.801428

Conflict of Interest: YQ, ZH, and SR were employed by the company China Petroleum Engineering and Construction Corporation Southwest Company.

The remaining author declares that the research was conducted in the absence of any commercial or financial relationships that could be construed as a potential conflict of interest.

Publisher's Note: All claims expressed in this article are solely those of the authors and do not necessarily represent those of their affiliated organizations, or those of the publisher, the editors and the reviewers. Any product that may be evaluated in this article, or claim that may be made by its manufacturer, is not guaranteed or endorsed by the publisher.

Copyright © 2022 Que, Hu, Ren and Jiang. This is an open-access article distributed under the terms of the Creative Commons Attribution License (CC BY). The use, distribution or reproduction in other forums is permitted, provided the original author(s) and the copyright owner(s) are credited and that the original publication in this journal is cited, in accordance with accepted academic practice. No use, distribution or reproduction is permitted which does not comply with these terms.